Steel and Composite Structures, *Vol. 30, No. 2 (2019) 149-169*
DOI: https://doi.org/10.12989/scs.2019.30.2.149

Further analysis on the flexural behavior of concrete-filled round-ended steel tubes

Fa-xing Ding [1,2], Tao Zhang [*1,2], Liping Wang [1,2] and Lei Fu [1]

[1] *School of Civil Engineering, Central South University, Changsha 410075, P.R. China*
[2] *Engineering Technology Research Center for Prefabricated Construction Industrialization of Hunan Province, 410075, P.R. China*

(*Received March 6, 2018, Revised December 19, 2018, Accepted January 21, 2019*)

Abstract. A new form of composite column, concrete-filled round-ended steel tubes (CFRTs), has been proposed as piers or columns in bridges and high-rise building and has great potential to be used in civil engineering. Hence, the objective of this paper presents an experimental and numerical investigation on the flexural behavior of CFRTs through combined experimental results and ABAQUS standard solver. The failure mode was discussed in detail and the specimens all behaved in a very ductile manner. The effect of different parameters, including the steel ratio and aspect ratio, on the flexural behavior of CFRTs was further investigated. Furthermore, the feasibility and accuracy of the numerical method was verified by comparing the FE and experimental results. The moment vs. curvature curves of CFRTs during the loading process were analyzed in detail. The development of the stress and strain distributions in the core concrete and steel tube was investigated based on FE models. The composite action between the core concrete and steel tube was discussed and clarified. In addition, the load transfer mechanism of CFRT under bending was introduced comprehensively. Finally, the predicted ultimate moment according to corresponding designed formula is in good agreement with the experimental results.

Keywords: concrete-filled round-ended steel tube (CFRT); flexural behavior; numerical investigation; composite action; stress redistribution

1. Introduction

Over the past several years, concrete-filled steel tubular (CFT) tubes have been increasingly used in bridges and high-rise building as piers or columns, which ideally combine the advantages of both steel and core concrete: namely high strength, high ductility and fast construction (El-Heweity 2012, Yuan *et al*. 2013, Chen and Wang 2015). The infill concrete adds stiffness to the steel tube and prevents the occurrence of local buckling, while the steel tube improves the compressive strength and deformation performance of the core concrete. Besides, the CFT require no reinforced cage and no formwork, because the steel tube can sever as formwork. With these advantages, CFT has more gained more attention of researchers (Aslani *et al*. 2015, Kim *et al*. 2013, Wan and Zha 2016, Wang and Chang 2013).

To date, the large aggregation of numerical and experimental studies on the flexural behavior of CFTs has been conducted in literature. Chen *et al*. (2016) carried out the experiments on thin-walled dodecagonal section double skin concrete-filled steel tubes under bending, and a design method was proposed. Chitawadagi and Narasimhan (2009) conducted the experiments on circular steel tubes filled still tubes and investigated the effect of different parameters on behavior of CFT. Han *et al*. (2006) reported the flexural behavior of circular section CFTs, and the design formula was proposed. Moon *et al*. (2012) studied the flexural performance of CFT members with circular sections using Finite element method, and a simplified model to predict the moment-drift relationship of CFST was proposed. Uenaka *et al*. (Uenaka *et al*. 2008, Uenaka and Tsunokake 2016) studied experimental on the flexural behavior of concrete filled double skin circular tubular. Wang *et al*. (2014) presents a finite element analysis to study the flexural performance of rectangular concrete filled steel tubular members, and the composite action between the core concrete and steel tube is discussed.

With the development of heavy haul railway and highway bridges, requirements for the bearing capacity, ductility and stiffness of the pier become higher. A new form of composite section, concrete-filled round-ended steel tubular section (CFRT), was proposed as shown in Fig. 1 and has already been applied in bridges (Xie *et al*. 2010, 2011), such as the Platform of the Xinglin Gulf in Xiamen City (China) and the Houhu Cable-stayed Bridge in Wuhan City (China). The CFRTs has a good external model, and meet the requirement of architectural esthetics, which can effectively reduce the impact of fluid load on the pier attributing to the semi-circle cross-section at the corners. However, up to now there is relatively little research reported on the flexural behavior of CFRTs and that mainly focused on axial loading. Ding *et al*. (2015, 2016) studied the CFRT columns and track-shaped rebar stiffened concrete-filled round-ended steel tube (SCFRT) columns experimentally, and investigated the effects of several key

*Corresponding author, Ph.D., Professor,
E-mail: zhangtao0226@csu.edu.cn

ISSN: 1229-9367 (Print), 1598-6233 (Online)

parameters, including the concrete strength, steel strength, steel ratio and aspect ratio, on the behavior of the columns. The composite action between the steel tube, core concrete and rebar was investigated. Finally, a practical formula for predicting the ultimate bearing capacity was established. In addition, the influence of some key parameters, including the concrete strength, steel strength, steel ratio and aspect ratio, on the flexural behavior of CFRTs was investigated and design formula was established to predict the ultimate moment (Ding *et al*. 2017). The above analysis can provide a basis for investigating the flexural performance of CFRTs. Nonetheless, the stress redistribution in the steel tube and core concrete, and composite action between the steel tube and core concrete still need to be clarified in the whole loading stage for CFRTs.

Experimental study have been a basic analysis method on investigating the behavior and predicting the response of steel-concrete composite structural, while finite element methods become more and more important, because which can simulate the case that are difficult or/and complex. Chang *et al*. (2013, 2014, 2016) studied the behavior of composite structures and rock structures using ABAQUS. Hassanein *et al*. (Hassanein *et al*. 2013, Hassanein and Kharoob 2014) performed finite element analysis to study behavior of circular concrete-filled double skin tubular short columns with external stainless steel tubes under axial loading. Pagoulatou *et al*. (2014) presented a numerical study on the behavior of circular concrete-filled double-skin steel tubular stub columns under concentric axial loads. Hence, this paper will be an attempt to analyze the behavior of CFRTs in detail by the ABAQUS program.

With consideration of the research gaps as mentioned above, this paper is devoted to further investigating the flexural behavior of CFRTs using ABAQUS based on the existed research Ding *et al*. (2017). More specifically, based on the theoretical and numerical research in the research team, the main contents of this paper are listed below: (1) Flexural tests on seven specimens were designed to investigate the behavior of CFRTs. (2) Experimental data are adopted to verify the accuracy of Finite element (FE) models, including the material constitutive model of concrete and steel, element type, mesh and boundary condition. (3) Based on the FE results, the moment vs. curvature curves and failure modes during the loading process are analyzed in detail. The FE models are used to investigate the development of the stress and strain distribution in the core concrete and steel tube, and the composite action between the steel tube and core concrete is discussed. (4) The load transfer mechanism in the core concrete and steel tube is introduced in detail.

2. Experimental investigation

2.1 Description of test specimens

To investigate the flexural behavior of the concrete-filled round-ended steel tubes (CFRT), a total of 7 specimens were designed in this study, and the parameters considered in the analysis included the loading direction (major axis and minor axis), the aspect ratio and the wall thickness of the steel tube. Fig. 1 shows the cross-section of concrete-filled round-ended steel tubes (CFRT), where B is the length of the specimen in the minor axis direction of the cross-section, D is the length of the specimen in the major axis direction of the cross-section and also the diameter of the semi-circle cross-section, t is the wall thickness of the steel tube. The detailed information on the specimens is listed in Table 1. The cross-section of CFRTs changed with the change of aspect ratio (B/D), which is defined herein as B divided by D. The cross-section of CFRTs with $B/D = 1$ is a circular CFT, namely concrete-filled circular tube (CFT), being a special case of CFRTs. The aim of the paper is to investigate CFRTs including both the special case (CFTs) and normal cases. L is the longitudinal dimension of the specimen.

In this study the test specimens were labeled such that the type of the specimens, the loading direction, the aspect ratio and the nominal thickness of the steel tube can be identified from the label. For example, the label “R-Ma-2-

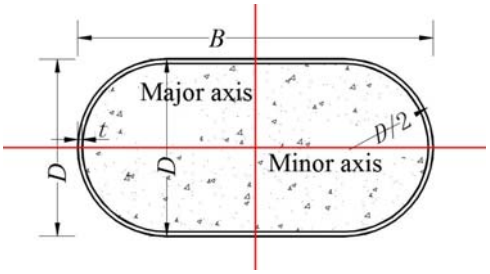

Fig. 1 Cross-section of the CFRTs

Table 1 Geometrical and material parameters for FE model

Specimen ID	$B\times D\times t$ mm	B/D	L mm	ρ	f_{cu} Mpa	f_y Mpa	f_u Mpa	E_s Mpa	ν_s
R-1-3	200×200×3.04	1	2000	0.060	38.75	353	500	2.09×10^5	0.292
R-Ma-2-3	400×200×3.04	2	3000	0.043					
R-Ma-2-4	400×200×3.82	2		0.054		336	442	2.02×10^5	0.256
R-Ma-3-3	600×200×3.03	3	4000	0.039		353	500	2.09×10^5	0.292
R-Mi-2-3	400×200×3.01	2	3000	0.043					
R-Mi-2-4	400×200×4.01	2		0.057		336	500	2.02×10^5	0.256
R-Mi-3-3	600×200×2.98	3	4000	0.038		353	442	2.09×10^5	0.292

3" defined the specimens as follow: the first letter indicates the cross-section type of the specimens, where the prefix letter "R" refers to concrete-filled round-ended steel tube. The following two digits "Ma" indicate loading direction. The following digits "2" refers to the aspect ratio. The last digit "3" is the nominal thickness of the steel tube in mm.

The tested specimens were fabricated in two steps. Firstly, the flat steel plate was molded into U-shaped sections. And then two U-shaped were welded together with single bevel welds. Butt welds were used according to the standard GB 50017-2003 and it was also necessary to ensure that the sites of welding were smooth after welding. Before pouring concrete, the inside surfaces of the steel tube were brushed to remove any rust and loose debris present, and the deposits of grease and oil, if any, were cleaned away. Then the cover plate was initially welded to one end of the steel tube, and make the steel tube erect. Concrete was placed from the top of the steel tube, and carefully vibrated by a vibrator to distribute the concrete evenly inside the steel tube. The upper and lower surfaces of concrete and steel tubular were smoothed. Meanwhile, the standard concrete cubes with a dimension of 150 mm were prepared and cured under the same condition as the concrete used in specimens. Finally, for better observation and record of deformation and failure modes of the specimens, the red paint was sprayed on the outer surface of the steel tube and the white grids of 50 mm × 50 mm were plotted on the painted surface.

2.2 Material

Before the tests, the mechanical properties of the respective steel and concrete were tested in accordance with the corresponding the Chinese standard. Mild steel was adopted in the study and three tensile coupons were conducted to obtain the material properties according to the standard GB/T228-2002. The obtained yield strength, ultimate tensile strength, elastic module and Poisson's ratio of steel are listed in Table 1. Besides, the cubic compressive strength of concrete was measured according to the standard GB/T50081-2002 and their compressive strengths were 38.75 MPa.

2.3 Measuring point arrangement and experimental setup

All the tests were conducted under four-point bending with simply supported condition in the National Engineering Laboratory for high-speed railway construction technology of Central South University. The load was applied to the specimens using the 50 t hydraulic jack. To accurately measure the deformation, strain rosettes were attached around the outer surface of the steel tube at the mid-span and three LVDTs were placed under the mid-span and two loading points of the specimen, respectively. In addition, two dial indications were fixed at the two ends of the specimen to measure the displacement of the test frame during the test, as shown in Fig. 2(a).

The test was carried out using load control in the elastic stage, with a force increment of 1/20 of the predicted ultimate load. After the load reached 70% of the predicted ultimate bearing capacity, the test was switched to displacement control with an increment of 0.2 mm until the predicted ultimate load was reached. The specimens were loaded at a step of 0.5 mm and maintained 5 min for each step in the post-ultimate stage. A data acquisition system

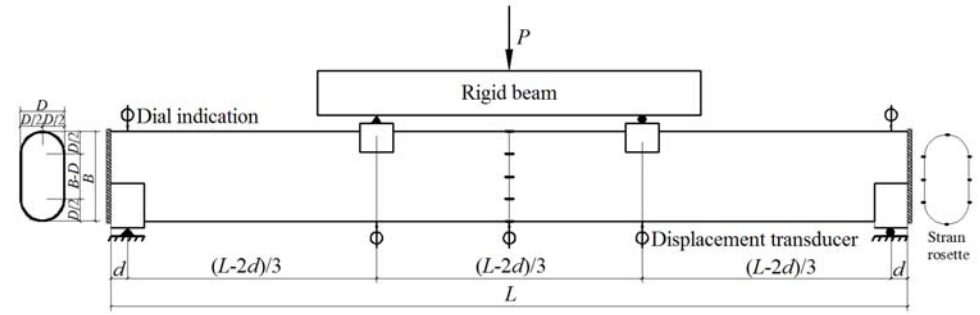

(a) Schematic view

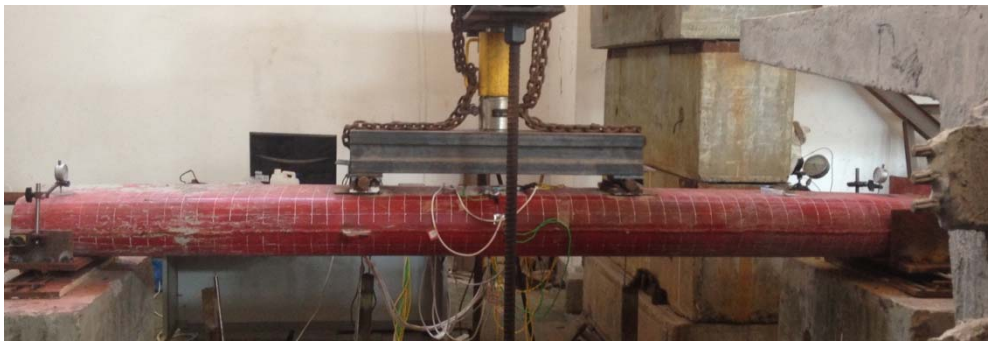

(b) Experimental setup

Fig. 2 Experimental instrumentation for all specimens

was used to record the applied load and the reading of the transducers and strain rosettes at regular intervals during the tests. When the mid-span deflection of the specimen reached about 3% of the length of the specimen, the test was stopped. Fig. 2(b) gives an overall view of the experimental setup.

3. Experimental result and discussion

3.1 Load vs. deflection curves

Based on the test observation and the obtained moment vs. deflection curves of per CFRT, as presented in Fig. 3, the load vs. displacement curves consisted of three parts including the ascending, descending and stable part. The ascending part could be separated into elastic and plastic stages.

Stage I: At the initial loading stage, all the specimens were in elastic stage as indicted by the linear responses of the moment vs. displacement curves, where the moment increased quickly, whereas the increase of the deflection was very small.

Stage II: The steel tube began to yield and the moment vs. displacement curves demonstrated elastic-plastic behavior, when the applied load reached about 70% of the ultimate load. At same time, the stiffness of the specimens deviated from its initial value.

Stage III: The moment of the tested specimens almost remained constant and tended to stabilize, while the mid-span deflection increased sharply. No obvious descending was observed in the curves, indicting the specimens under

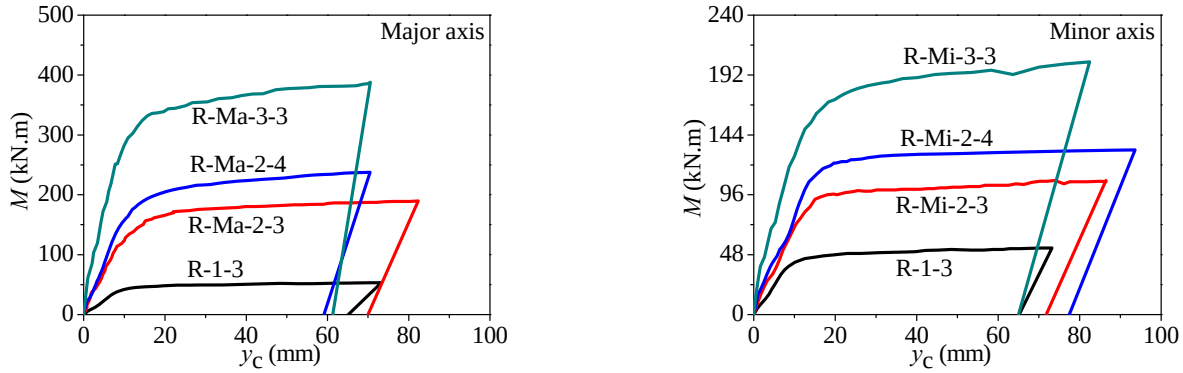

(a) Major axis (b) Minor axis

Fig. 3 Comparison of the moment vs. mid-span deflection curves

Fig. 4 Typical failure modes for all tested specimens

bending all behaved in a very ductile manner.

3.2 Failure modes

Theoretically speaking, when the mid-span deflection of the specimens reaches about 3% of the length of the specimen which are considered to reach the failure criteria, the specimen failed. Fig. 4 shows the typical failure modes of CFRT. The failure mode of CFRTs showed an outward folding failure mechanism and the specimen failed in a very ductile manner. It can be seen that the failure mode of CFRT under bending at major axis is the same as that under bending at minor axis, which revels the bending direction (major or minor axis) has no obvious effect on the failure modes of CFRTs.

Moreover, it should be noted from Fig. 5 that some local buckling on specimens under bending at the major and minor axis in pure bending segment were observed, while the deformation of local buckling at the minor axis was greater than that at the major axis, indicating that the confinement effect of the steel tube on the core concrete at the major axis was superior to that at the minor axis. The confinement effect decreases gradually at the position of local buckling, where the decrease in the confinement effect resulted in the core concrete in uniaxial compressive stress at the position of local buckling. The outer steel tube was removed from the core concrete after the tests. It can be observed that the core concrete at the local buckling zone was cracked due to the reduction of the confinement effect of the steel tube, but the core concrete remained its entirety

(a) Major axis (b) Minor axis

Fig. 5 Comparison of failure modes between major and minor specimens

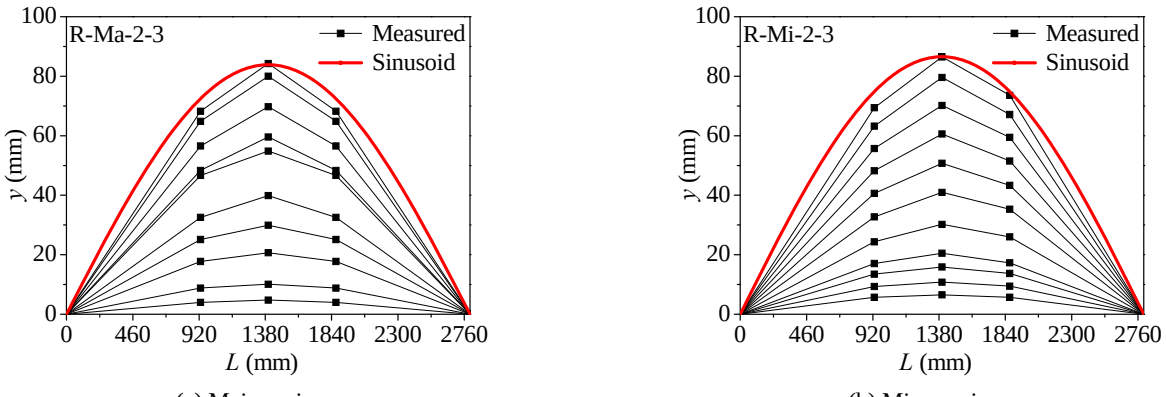

(a) Major axis (b) Minor axis

Fig. 6 Typical deflection of the specimens

due to the confinement effect of the outer steel tube. Furthermore, the outer steel tube was removed to observe the deformation of the core concrete after experiments. It can be found that the vertical cracks of the core concrete below the neutral axis were observed and distributed uniformly in pure bending segment.

Fig. 6 shows two typical set of deflection curves of CFRTs. It is clear from Fig. 6 that the deformation at both sides of mid-span is symmetric during the loading process, and the predicted deflection curves are both in the shape of a half-sine wave, which reveals that the means of loading and the deformation process are reasonable.

Fig. 7 gives the moment vs. strain curves for R-Ma-2-3 and R-Mi-2-3 specimen at different points. Based on the careful observation for Fig. 7, the strain in the compression and tensile zone increased linearly and slowly at the initial stage of loading, and the strain in the tensile zone was obviously greater than that in the compression zone. Besides, the yield of the steel tube in the tensile zone occurred earlier than that in the compression zone. What's more, those curves can reflected such tendency that the neutral axis gradually moved upwards with the increase of the load. Besides, the compressive state at 3 point of the steel tube was transformed into the tensile state.

Fig. 8 shows the longitudinal strain distribution along the height of the cross section of specimens, where the strain are defined as negative in compression zone and positive in tensile zone, respectively. It is found from Fig. 8 that the strain development in tension zone was greater than that in the compression zone, which could be induced by the compressive stress of the core concrete in compression zone. In addition, with the increase of load, the neutral axis gradually moved upwards from the centroidal axis of cross-section, which coincides with the Fig. 7. The intersecting point of the mid-span strain curves represented the position of neutral axis of the plane. The results were consistent with the assumption of planar cross-section behavior at the mid-span of the specimens.

3.3 Parametric study

3.3.1 The effect of the steel ratio

The steel ratio (ρ_s), defined as the steel area (A_s) divided by the total cross-sectional area (A_{sc}), is a key parameter, which has been extensively investigated in previous research of CFT members.

Fig. 9 gives the comparisons of the ultimate moment for all the tested specimens. The steel ratio is variable and other parameters are kept the same as mentioned above. From Fig. 9, it can be found that with the increase of steel ratio from 0.043 to 0.054, the ultimate moment of the R-Ma-2-4 specimen was improved by 23% compared to the R-Ma-2-3 specimen. Meanwhile, in comparison to the R-Mi-2-3, the ultimate moment of the R-Mi-2-4 was improved by 26% with the increase of the steel ratio from 0.043 to 0.057. Hence, the comparison clearly reflects that increasing the

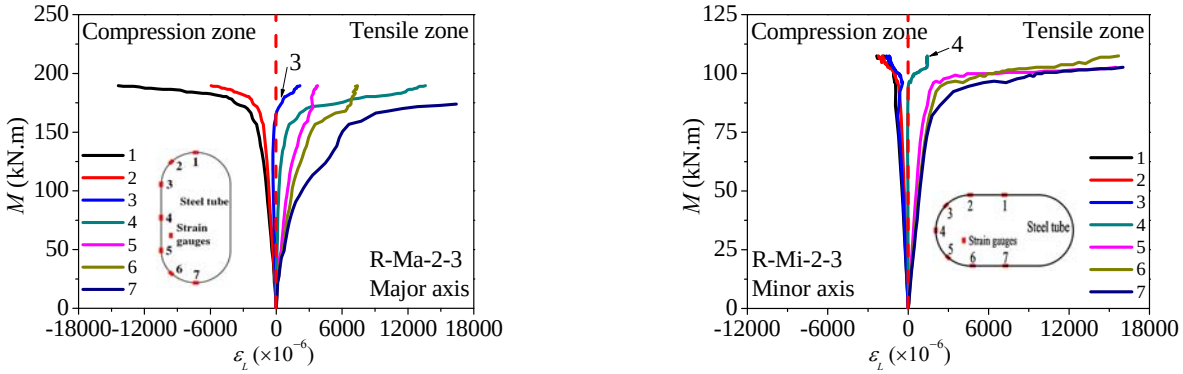

(a) Major axis (b) Minor axis

Fig. 7 The moment vs. strain curves at different points of specimens

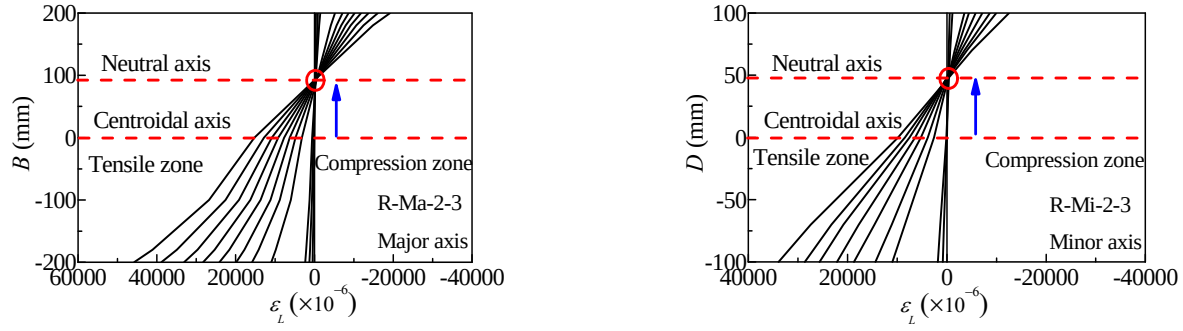

(a) Major axis (b) Minor axis

Fig. 8 Strain distribution at mid-height of specimens

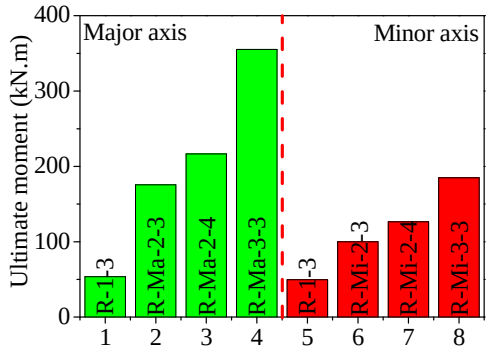

Fig. 9 Comparison of ultimate moment for all specimens

steel ratio contributes to improve the ultimate moment for the specimens under bending.

3.3.2 The effect of the aspect ratio (B/D)

In this section, the parameter "aspect ratio (*B*/*D*)" is defined herein as the *B* divided by *D*, where the aspect ratios (*B*/*D*) are 1, 2 and 3, respectively. Compared to the R-1-1 specimens, the ultimate moment of the R-Ma-2-3 and R-Ma-2-4 were improved by 2.29 times and 5.66 times respectively, as the aspect ratio increases. Besides, in comparison to R-1-1 specimens, the ultimate moment of the R-Mi-2-3 and R-Mi-2-4 were improved by 0.87 times and 2.47 times respectively, with the increase of the aspect ratio. Therefore, it can be concluded that the aspect ratio (*B*/*D*) has obvious influence on the ultimate moment.

From the above analysis, it can be found that the results of comparisons coincide with the results investigated by Ding *et al*. (2017).

4. Finite element (FE) modeling

4.1 Finite element mesh and boundary conditions

Finite element (FE) models are established using the finite element package ABAQUS (Hibbitt *et al*. 2003). In these models, the 8-node reduced integral format 3D solid element (C3D8R) is adopted to model the core concrete, steel tube and cover plate for all specimens. The structured meshing technique is adopted. Mesh convergence studies are first performed to ensure that the FE mesh is sufficiently fine to give accurate results and secondly to guarantee the computational efficiency. A surface-based interaction with "hard" contact in the normal direction and the Coulomb friction coefficient of 0.5 in the tangential direction of the interface is used to simulate the interfacial behavior between the steel tube and core concrete, in which the sliding formulation is finite sliding. The steel tube is chosen as the master surface, and the core concrete is chosen as the slave surface. A tie constraint may couple two separate surfaces so that no relative motion would occur. Therefore, the tie option is adopted for the constraint between the cover plate and the concrete as well as the steel tube at two ends of the specimens.

The model is loaded under four-point bending, which is consistent with the tests. In the FE model, both the support and loading plates are modeled as rigid bodies. The simply supported boundary condition is modeled by releasing the in-plane rotation at the reference point 1, and releasing both the in-plane rotation and axial displacement along the specimen at the reference point 2. Considering the nonlinear calculation is more easily convergent under displacement loading, the load is applied to the specimen through the loading plates (reference point 3) by means of a specified displacement. The boundary conditions and meshing results of the FE model with the structured meshing technique are shown in Fig. 10.

4.2 Material constitutive model

The concrete damaged plasticity model and Willam-Warnke five-parameter failure criteria in ABAQUS (Hibbitt *et al*. 2003) were adopted in the FE modeling for the concrete. The following stress-strain relationship of concrete under uniaxial compression proposed in (Ding *et al*. 2011) is used in the model.

$$y = \begin{cases} \dfrac{kx + (m-1)x^2}{1 + (k-2)x + mx^2} & x \le 1 \\ \dfrac{x}{\alpha_1 (x-1)^2 + x} & x > 1 \end{cases} \tag{1}$$

where $y = \sigma/f_c$ and $x = \varepsilon/\varepsilon_c$ are the stress and strain ratios of the core concrete to the uniaxial compressive concrete respectively. σ and ε are the stress and strain of the core concrete. $f_c = 0.4 f_{cu}^{7/6}$ is the uniaxial compressive strength of concrete, where f_{cu} is the compressive cubic strength of concrete. ε_c is the strain corresponding with the peak

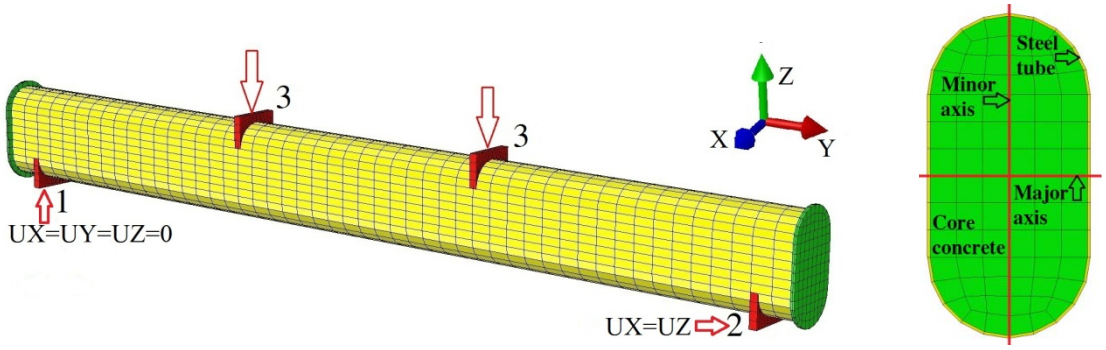

Fig. 10 FE model after meshing

compressive stress of concrete, where $\varepsilon_c = 383 f_{cu}^{7/18} \times 10^{-6}$. The parameter k is a ratio of the initial tangent modulus to the secant modulus at peak stress and equals to $9.1 f_{cu}^{-4/9}$. m is a parameter that controls the decrease in the elastic modulus along the ascending portion of the axial stress-strain relationship and equals to $1.6(k\text{-}1)^2$. For a steel-concrete composite beam, parameter α_1 is can be taken as 0.15. The Poisson ratio v_c of concrete is taken as 0.2.

The triaxial plastic-damage constitutive model of concrete adopted in this paper was based on the stress-strain relation of concrete under uniaxial stress, together with the parameters of concrete strength criterion under multi-axial stresses and other parameters stated while it had no relation to the material and shape of tube.

And the relevant parameters used for this material model were defined in ABAQUS according to Ding *et al.* (2011), as follow: the eccentricity is 0.1; the ratio of initial equibiaxial compressive yield stress to initial uniaxial compressive yield stress is 1.225; the ratio of the second stress invariant on the tensile meridian to that on the compressive meridian is 2/3; the viscosity parameter is 0.005; and the dilation angle is 40°. More information of the concrete model can be referred in (Ding *et al.* 2011). These parameters have been validated by experimental results (Ding *et al.* 2015-2017, Liu *et al.* 2016), where the adopted stress-strain relationships of concrete in compression and tension are applicable for concrete with strength ranging from 20 to 140 MPa.

Therefore, concrete model and parameters available above mentioned, in which the composite action between the core concrete and steel tube is considered, is suitable for numerical analysis in concrete-filled round-ended steel tubes.

An elasto-plastic model, with consideration of Von Mises yield criteria, Prandtl-Reuss flow rule, and isotropic strain hardening, was used to describe the constitutive behavior of steel. The model has been validated in prior studies (Ding *et al.* 2011), and described as follows

$$\sigma_i = \begin{cases} E_s \varepsilon_i & \varepsilon_i \le \varepsilon_y \\ f_s & \varepsilon_y < \varepsilon_i < \varepsilon_{st} \\ f_s + \zeta E_s (\varepsilon_i - \varepsilon_{st}) & \varepsilon_{st} < \varepsilon_i \le \varepsilon_u \\ f_u & \varepsilon_i > \varepsilon_u \end{cases} \quad (2)$$

where, σ_i and ε_i are the equivalent stress and strain of steel. f_y, and f_u (= $1.5 f_s$) are the yield strength and ultimate strength respectively. E_s (= 2.06×10^5MPa) and E_{st} ($E_{st} = \zeta E_s$) are the elastic modulus and strengthening modulus. ε_y, ε_{st} and ε_u are the yield strain, hardening strain, and ultimate strain of steel, which is expressed by $\varepsilon_u = \varepsilon_{st} + 0.5 f_s/(\zeta E_s)$, where $\varepsilon_{st} = 12\varepsilon_b$, $\varepsilon_u = 120\varepsilon_b$ and $\zeta = 1/216$.

4.3 Verifications of the FE modeling

According to the material model and boundary condition as mentioned above, the accuracy of numerical analysis results obtained from established FE models were standardized against the corresponding experimental results in this paper. The moment vs. deflection curves, ultimate moment and failure modes executed by FE models were compared with the experimental results for validation purpose.

4.3.1 The moment vs. deflection curves and ultimate moment

Fig. 11 shows the comparisons of the moment vs. mid-span deflection curves between experimental and corresponding FE results, which reveals that the moment vs. mid-span deflection curves of specimens under bending are divided into three stages: the elastic stage, elastic-plastic stage and plastic stage. In the elastic stage, the crack of concrete led to reduction in the stiffness of the specimens in experiments, whereas, the concrete crack under low stress is neglected in FE model. Therefore, there is slight difference in the elastic stiffness between experimental and FE result. In the elastic-plastic stage and plastic stage, the experimental curves are consistent with the corresponding FE results. And there is no obvious descending in the plastic stage till reaching the ultimate strength, which indicates that the specimens behave in a very ductile manner. Therefore, it can be concluded from Fig. 11 that the numerical simulation accurate reflects the development of the specimens, and the predicted curves agree reasonably well with the experimental results and the discrepancies of the ultimate moment (M_u) between experimental and corresponding FE results are less than 8% for all the specimens.

Besides, existing experimental data (Ding *et al.* 2017, Han *et al.* 2006) was also collected to further verify the

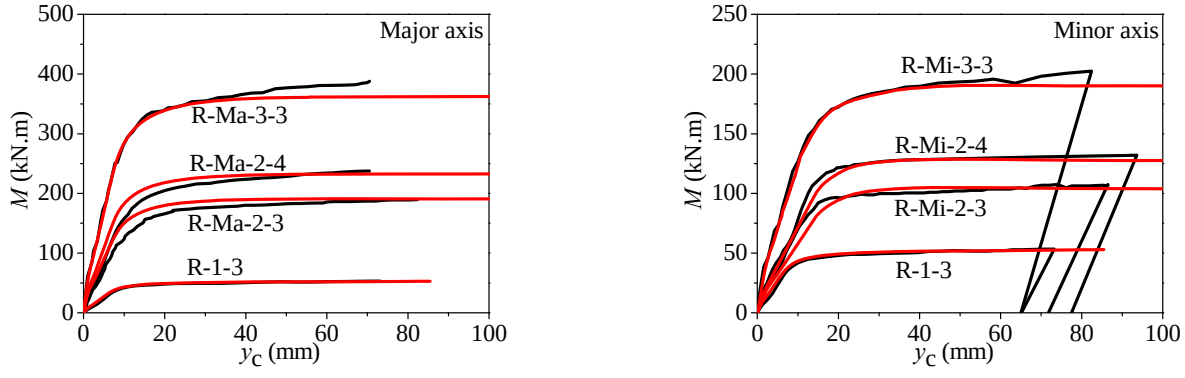

(a) Major axis (b) Minor axis

Fig. 11 Comparison of moment vs. deflection curves between FE and experimental results

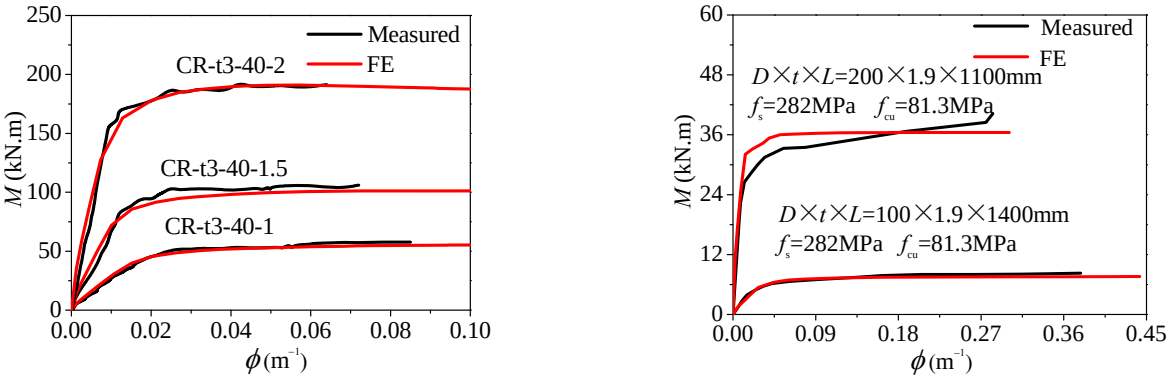

(a) by Ding *et al*. (2017) (b) by Han *et al*. (2006)

Fig. 12 Comparison of moment vs. curvature curves between experimental and FE results

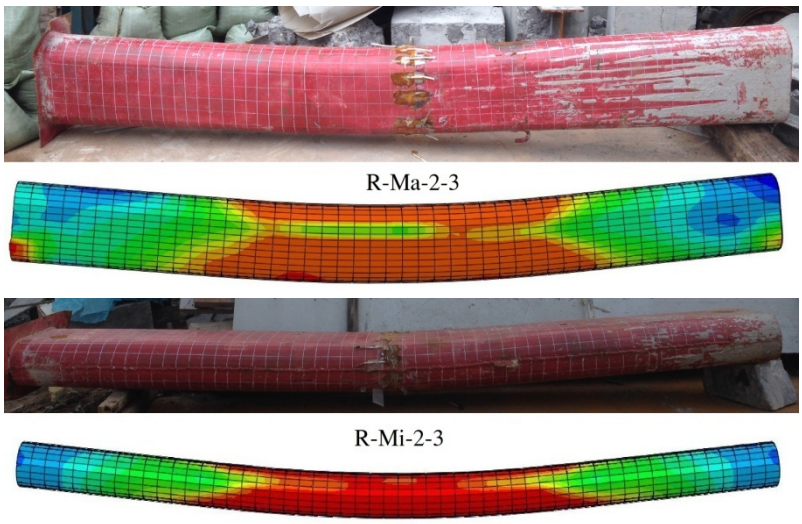

Fig.13 Comparison of failure modes between test and FE results

accuracy of the established FE model, as shown in Fig. 12. It is shown that the FE modeling curves match the experimental results well, especially for the elastic stage and ultimate bearing capacity.

4.3.2 Failure mode

In addition, the comparisons of failure modes between experimental and FE results are shown in Fig. 13. The failure modes for both experimental and FE results are an outward folding failure mechanism and the all the specimens exhibits a significant ductility. It is observed that the failure mode of experimental results coincides with that of FE results. Therefore, the FE model and the material constitutive model adopted in this study were proved to be reasonable and adequate.

5. Flexural behavior analysis and discussion

In order to obtain deeper understanding on the flexural behavior of CFRTs, the predicted moment vs. curvature curves during the loading process and failure modes are investigated, and the composite action between the core concrete and steel tube is discussed. The FE models are established to analyze the development of the stress and strain distribution of the steel tube and core concrete. The following will take the R-Ma-2-3 and R-Mi-2-3 specimen as examples to discuss the flexural behavior of CFRTs.

5.1 Complete curve analysis

The typical predicted moment vs. curvature curve of the CFRT is shown in Fig. 14. Based on the observation of the predicted moment vs. curvature curve of CFRT, as shown in Fig. 14, the specimens generally are considered to experience three stages under bending until failure: elastic stage (OB), elastic-plastic stage (BD), and plastic stage (DF). Several characteristic points are marked on the curve of CFRT, where point A is corresponding to the initial cracking of the core concrete in tensile zone; points B and C are corresponding to the initial yield of the steel tube in tensile and compression zone; the strain of the steel tube at points D and E in tensile zone reaches 0.01 and 0.02, respectively. The maximum strain of 0.01 (Han *et al*. 2006) is defined as the ultimate bending moment (M_u) of CFRTs.

Elastic stage (OB): The predicted moment vs. curvature

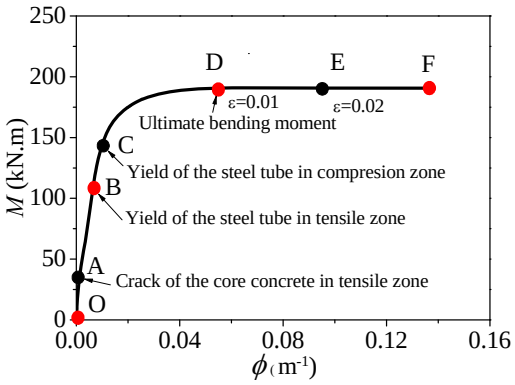

Fig. 14 The predicted moment vs. curvature curves

curve of the CFRT approximately remains straight line. The moment increases quickly, whereas the increase of curvature is very minimal. When the moment reaches point A, the initial cracking of the core concrete in tensile zone occurs. The cracking of the core concrete in tensile zone indeed leads to the degradation of flexural stiffness for CFRTs. Theoretically speaking, CFRTs behaves elastically only before the initial cracking of the core concrete in tensile zone. In general, the CFRT behaves a well elastic manner till the yield of the steel tube in tensile zone (point B). However, there exist bond and/or friction in the interface between the core concrete and steel tube, which can effectively prevent the development of the cracking concrete develops uniformly along pure bending zone in tensile zone. In addition, the cracking of the core concrete in tensile zone lead to reduction in the tensile stress of concrete (low tensile stress). Such reduction is compensated by the increase in tensile stress of steel in tensile zone due to the composite action between the steel tube and core concrete. Noticeable increase in stress of the steel tube can continue till yield of the steel tube in tensile zone. Therefore, it is concluded that the initial cracking of the core concrete and yield of the steel tube in tensile zone have almost no influence on the flexural stiffness of CFRTs, namely, the behavior approximately remains elastic.

Elastic-plastic stage (BD): the predicted moment vs. curvature curve begins to deviate from its initial stiffness and demonstrates nonlinear behavior. After the yield of the steel tube in tensile zone (point B), deformation of the CFRTs accelerates compared to the elastic stage, and as soon as the yield of the steel tube in compression zone (point C) occurs, the increase in curvature of CFRTs becomes obvious. The flexural stiffness in this stage is less than that in the elastic stage. It should be pointed out that the yield of the steel tube in tensile zone lead to acceleration in degradation of flexural stiffness for CFRTs, whereas the steel tube and core concrete in compression zone can offer strong support to resist deformation of CFRTs till the yield of the steel tube in compression zone. Actually, the yield of the steel tube in both tensile and compression zone allow more deformation of CFRTs. In addition, confinement effect of the steel tube on compression concrete increases after the

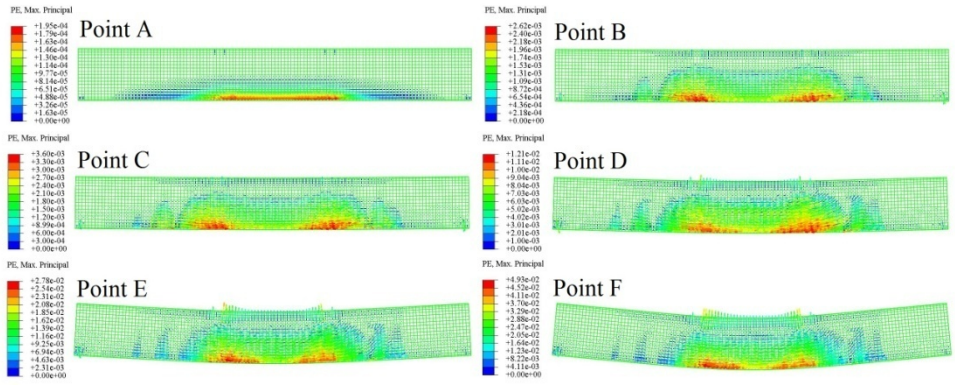

(a) Major axis

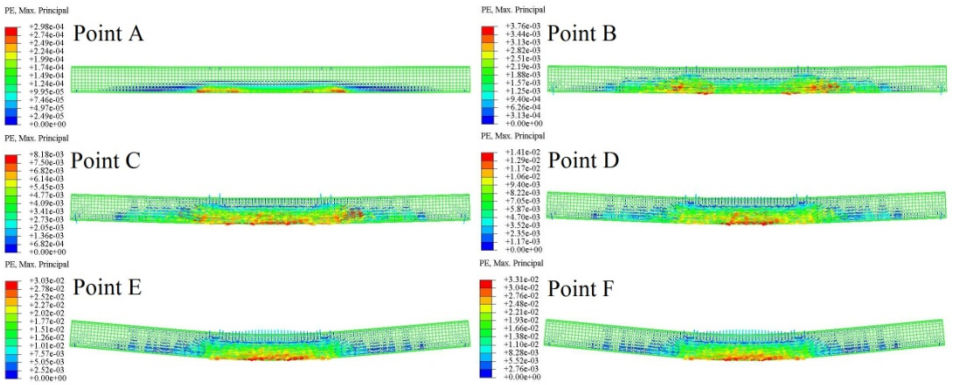

(b) Minor axis

Fig. 15 Development of plastic strain distribution in the core concrete

yield of the steel tube in compression zone. The moment of CFRTs still has a moderate increase till point E after the yield of the steel tube in compression zone (point C). Meanwhile, the gradual development in yield of the steel tube moves from the bottom and top fibers toward the neutral axis.

Plastic stage (DF): The increase in moment of CFRTs increases slightly and tends to become stable finally, whereas curvature of CFRTs increases sharply. There is no obvious descending in the curves of CFRTs, indicting the good ductility of the specimens under bending. The potential increase of moment is mainly influenced by the strain hardening effect of steel and stress redistribution in CFRTs.

5.2 Analysis on failure mode

The vector symbol in ABAQUS (Hibbitt *et al*. 2003) is adopted to visually illustrate crack of concrete in CFRT. It should be noted that cracks of concrete in the tensile zone depend on the maximum plastic strain and the crack of concrete is perpendicular to the plastic strain. The arrow and density of the maximum plastic strain vector symbol represent the direction of the plastic strain and the extent of concrete cracking, respectively. The more the plastic strain is, the more severe the crack of concrete is.

Fig. 15 gives the development of the plastic strain distribution in core concrete at different characteristic points. It can be seen that at point A, when the maximal plastic strain is about 0.0002, as expected that the initial crack of the core concrete in tensile zone distributes uniformly in pure bending segment and two obvious cracks close to the load points. And then, with the further increase of load, the cracking of the core concrete develops quick, and more and more cracks appear and propagate in pure bending segment. It should be noted that the cracks of the

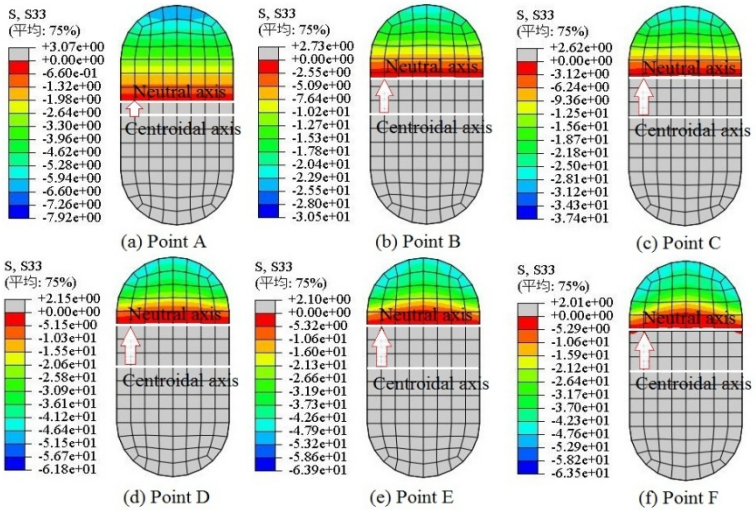

(a) Major axis

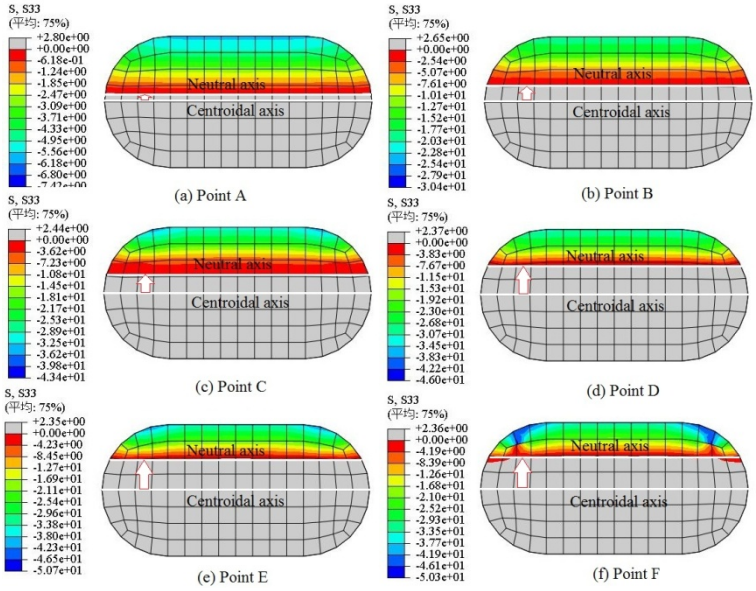

(b) Minor axis

Fig. 16 Development of the neutral axis at different stages of the core concrete

core concrete at the edge of pure bending segment in tensile zone develops more rapidly than others in pure bending segment during the loading process, and the zone of cracks propagate gradually toward the neutral axis. Moreover, no obvious shear cracks in the shear span are observed.

Fig. 16 clearly shows the development of the neutral axis at different stages of the core concrete. From another point of view, it can be found that the neutral axis coincide with the centroidal axis of the cross-section at the initial stage of load. Then, the neutral axis moves upwards from

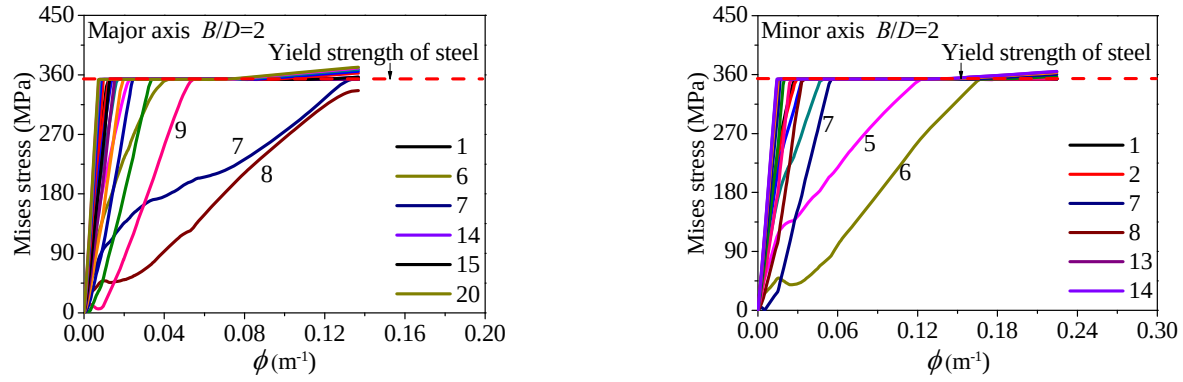

(a) Mises stress

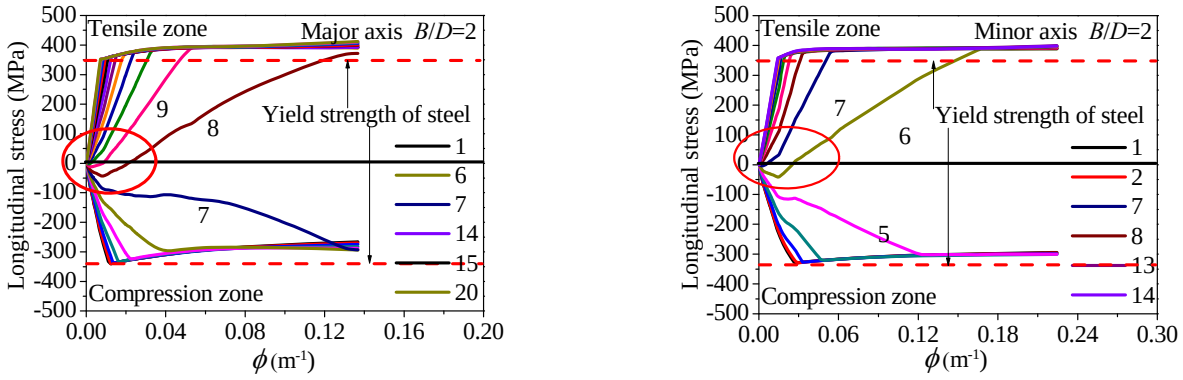

(b) Longitudinal stress

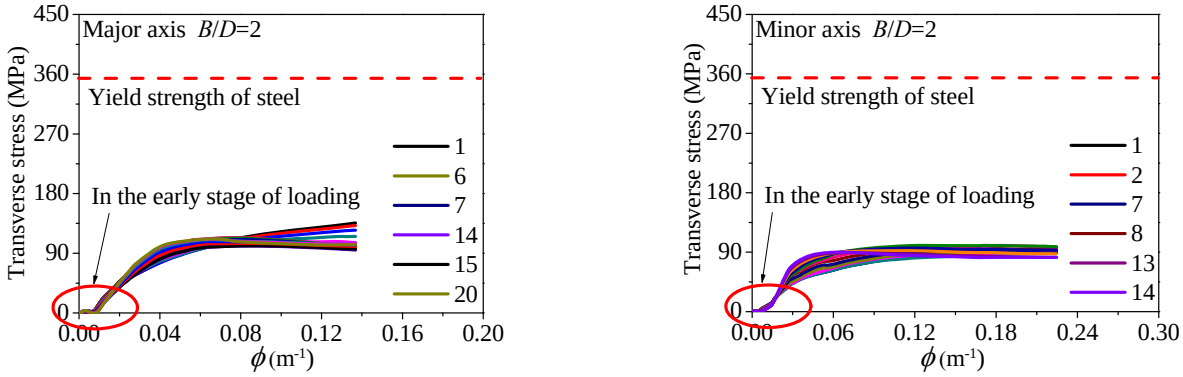

(c) Transverse stress

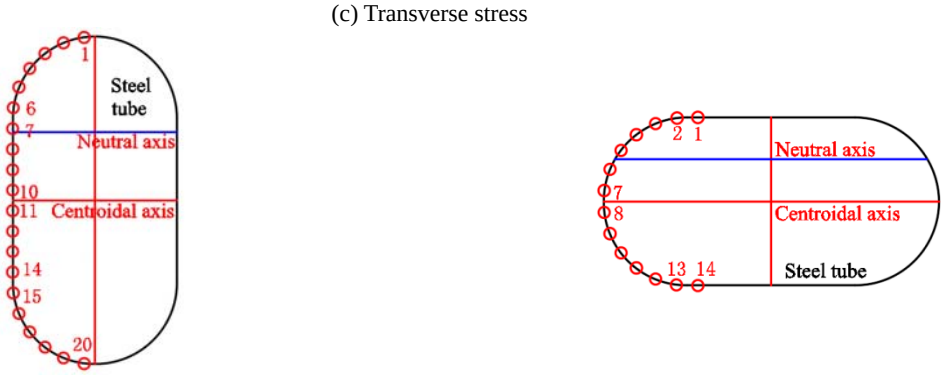

Fig. 17 Stress at mid-span section of the steel tube

the centroidal axis of the cross-section with the further increase of load until failure, which is consistent with the strain distribution of the steel tube, as shown in Figs. 6-7.

5.3 Development of stress in the steel tube and core concrete

Deformation of CFRTs increases as the load increases. In general, the stresses in the steel tube and core concrete also follow such tendency. However, there is no more increase and even decrease in stress with the further increase of deformation after reaching its peak stress, such as the yield of steel, the crush or cracking of concrete. At this point, the stress redistribution between the steel tube and core concrete in CFRTs occurs.

Fig. 17 shows the comparisons of stress vs. curvature curves of the steel tube at different points of mid-span section. From Figs. 17(a) and (b), it can be seen that the Mises and longitudinal stress of the steel tube at all points (apart from points 7, 8 and 9) in elastic stage increase faster until the yield of steel than that at points 7, 8 and 9 where the stress at point 8 don't reach the yield in the whole load process. This is because those points (points 7, 8 and 9) are the closest to the neutral axis. It should be pointed out that there is a moderate increase in longitudinal stress in tensile zone after the yield of steel, due to the stain-hardening effect of steel. In addition, it can be seen from Fig. 17(b) that the longitudinal stress of the steel tube at point 8 in compression zone gradually decrease until zero, and then that in tensile zone gradually increases till the yield of steel. That is to say that the neutral axis moves upwards with the increase of load, and the longitudinal compressive stress at point 8 is transformed into the longitudinal tensile stress. The transverse stress of the steel tube is very limited in the initial stage, and then increases slowly and tends to become stable finally, as shown in Fig. 17(c). The results illustrate that concrete and steel work independently in the early stage of loading. Similar conclusion can be drawn from Fig. 17 for CFRTs under bending at minor axis.

Fig. 18 gives the development of the Mises stress along the perimeter direction at the mid-span of the steel tube at different stages. It is obvious that the steel tube reaches gradually the yield of steel from the top and bottom of the cross-section to the neutral axis with the increase of load, while the steel tube near the neutral axis remains no yielding. Besides, Fig. 18 clearly demonstrates that the neutral axis of CFRTs is varied and moves gradually upwards.

Fig. 19 gives the development of the longitudinal stress in the steel tube along the length of specimens at different stages. As can be seen from Fig. 19(a), the whole up side of the steel tube is subjected to compressive longitudinal stress, and the compressive longitudinal stress in pure bending segment is obviously greater than that in the shear span segment. In addition, from Figs. 19(b) and (c), it can be seen that the whole mid and bot sides of the steel tube are subjected to tensile longitudinal stress, and the tensile longitudinal stress in pure bending segment is obviously

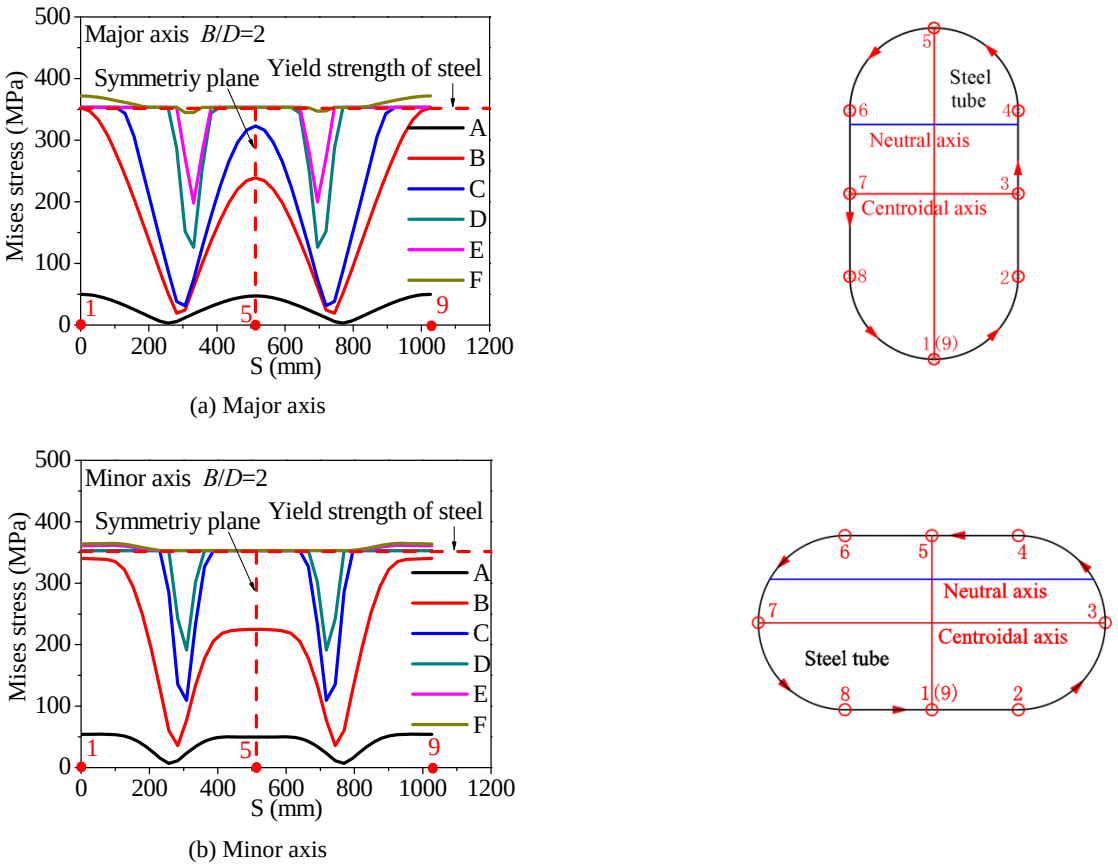

(a) Major axis

(b) Minor axis

Fig. 18 Development of Mises stress along the perimeter direction at different stages

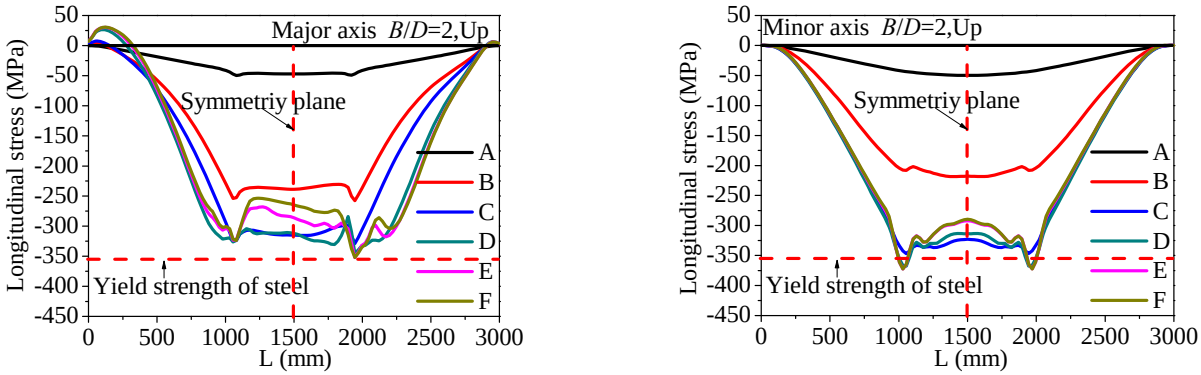

(a) Up

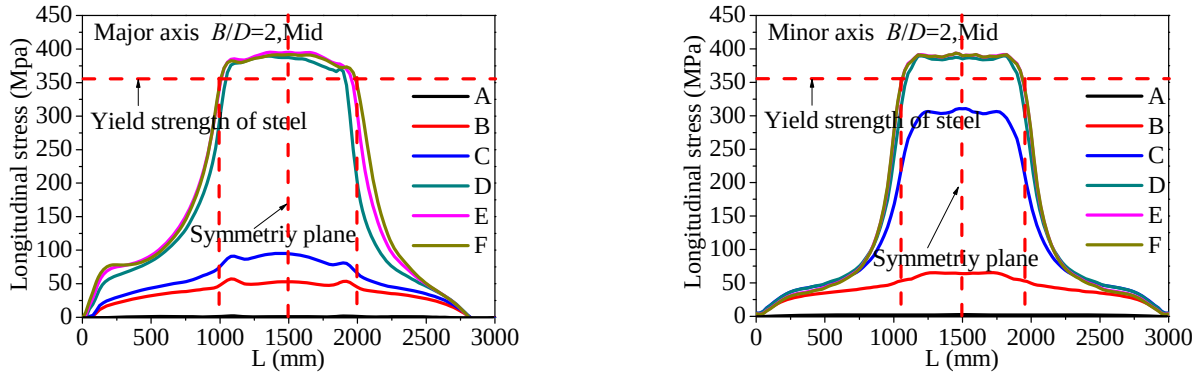

(b) Mid

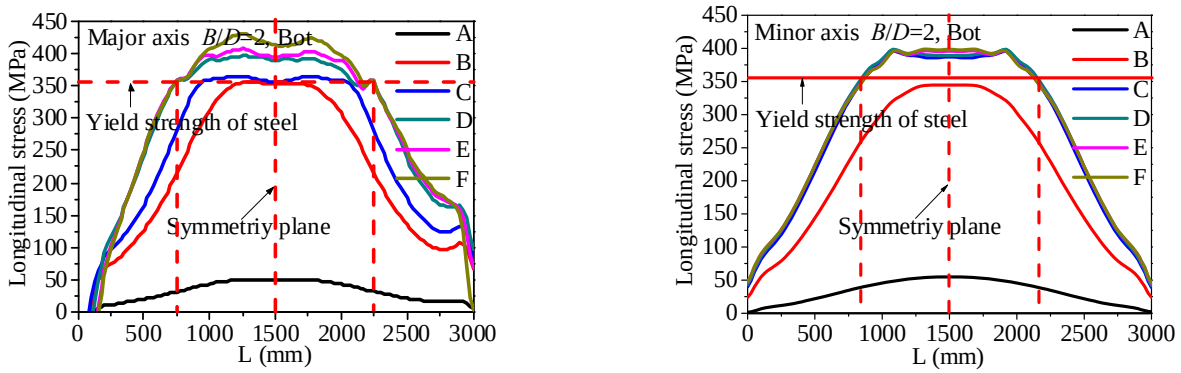

(c) Bot

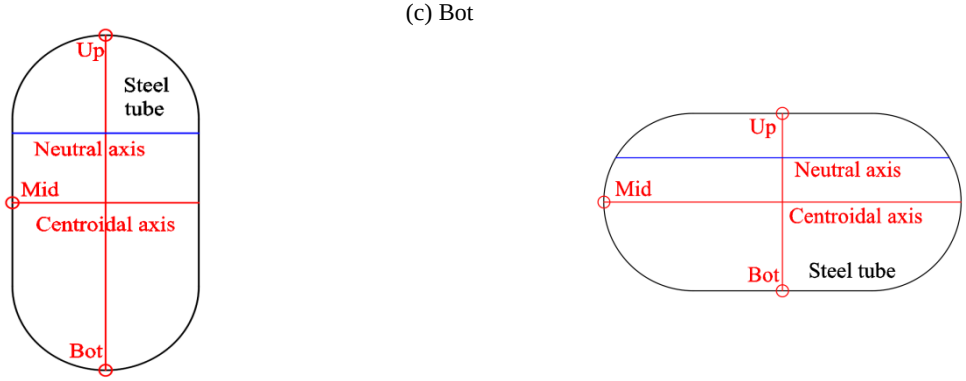

Fig. 19 Development of the longitudinal stress along the length of specimens at different stages

greater than that in the shear span segment. Meanwhile, the steel tube in the pure bending and part shear span segments reach the yield.

Fig. 20 shows the comparisons of longitudinal stress vs. curvature curves of the core concrete at different points of mid-span section. From Fig. 20, it can be found that the longitudinal stress of the core concrete at different points declines slowly after reaching its peak stress. With the neutral axis moving up, the longitudinal compressive stress of the core concrete at point 5 is transformed into the

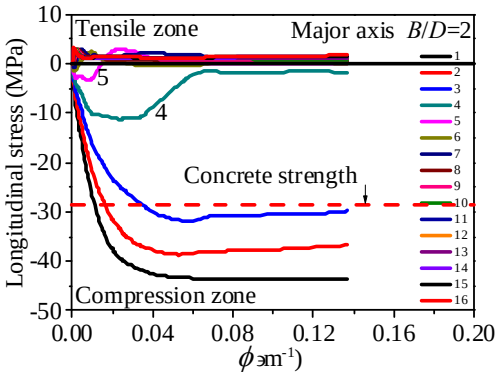

(a) Major axis

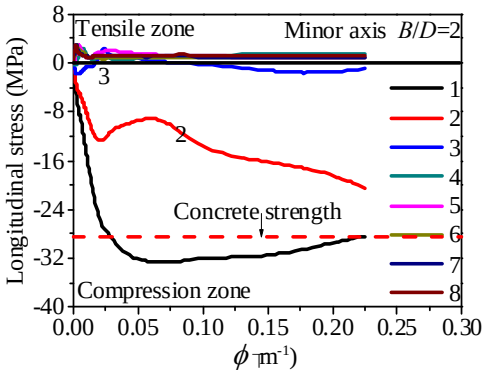

(b) Minor axis

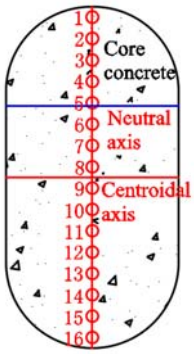

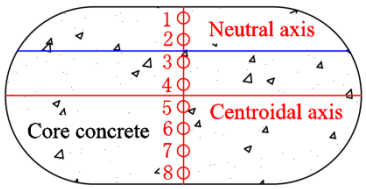

Fig. 20 Longitudinal stress at mid-span section of the core concrete

longitudinal tensile stress until cracking of the core concrete. That is to say that the stress state at point 5 transforms from the compressive stress to tensile stress, which is consistent with the results from Fig. 7 and Fig. 16. Moreover, the peak longitudinal compressive stress at point 1 is about 43.6 Mpa, which is obvious greater than the plain concrete. This is because the confinement effect of the steel tube on the core concrete helps in enhancing the compressive strength of concrete.

Fig. 21 gives the development of the longitudinal stress in the core concrete along the length of specimens at different stages. From Fig. 21(a), it can be observed that the whole up side of the core concrete is subjected to compressive longitudinal stress. In addition, the compressive longitudinal stress in pure bending segment is higher than that in the shear span segment, and the local stress concentration near the load point appear. From Figs. 21(b) and (c), the whole mid and bot sides of the core concrete are subjected to tensile longitudinal stress, while the core concrete near support points is under compressive longitudinal stress, which is very small.

Fig. 22 gives the development of longitudinal stress distribution in the core concrete along the longitudinal direction. No obvious change in the pattern of longitudinal stress distribution along the longitudinal direction of CRFTs is observed in the early stage of loading. However, the tensile zone of the core concrete develops gradually toward the support points and the maximum longitudinal compressive stress increases with the load increasing. And then the neutral axis moves gradually upwards. It can be seen that the maximum stress appears at load points and is as high as 62.1 Mpa, which is mainly induced by the local stress concentration near the load points rather than the overall structural response, as shown in Fig. 22. The maximum longitudinal compressive stress appears at load point and expands as a zone extending toward radial and circumferential directions. The core concrete below the neutral axis is severely cracked. The above analysis clearly demonstrates that the obvious stress redistribution in the core concrete generates during the loading process.

From the development of stresses in the core concrete and steel tube, it is strongly believed that the stress redistribution in the steel tube and core concrete is obviously influenced by the composite action between the steel tube and core concrete. The confinement effect of the steel tube on the compressive core concrete results in concrete in triple-axial compressive stress, but the confinement effect is passive and mainly depends on the stress state of steel. The confinement effect will decay after reaching the yield of steel. Therefore, it is concluded that the change of the composite action between the steel tube and core concrete results in the stress redistribution in specimens.

5.4 Composite action between the steel tube and core concrete

According to reference (Karimi *et al*. 2012), the Poisson's ratio is an important parameter for evaluating confinement effect. The strain ratio (v_{sc}) is defined herein as

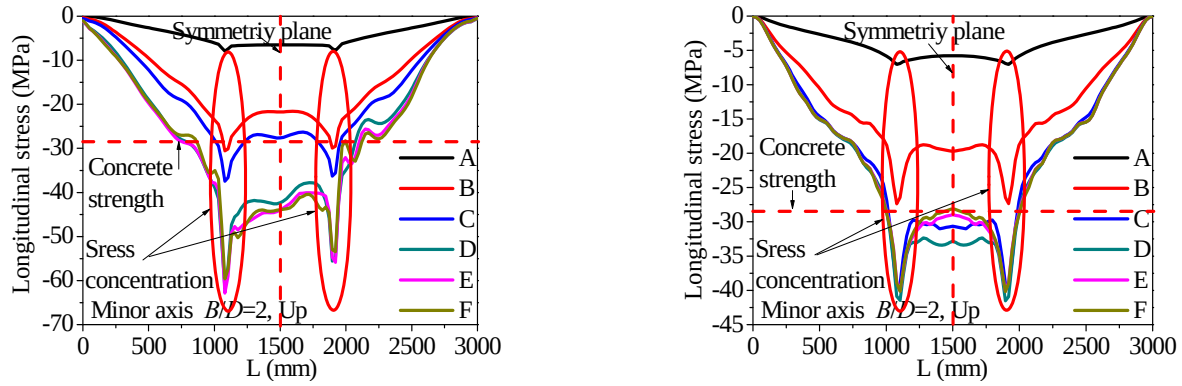

(a) Up

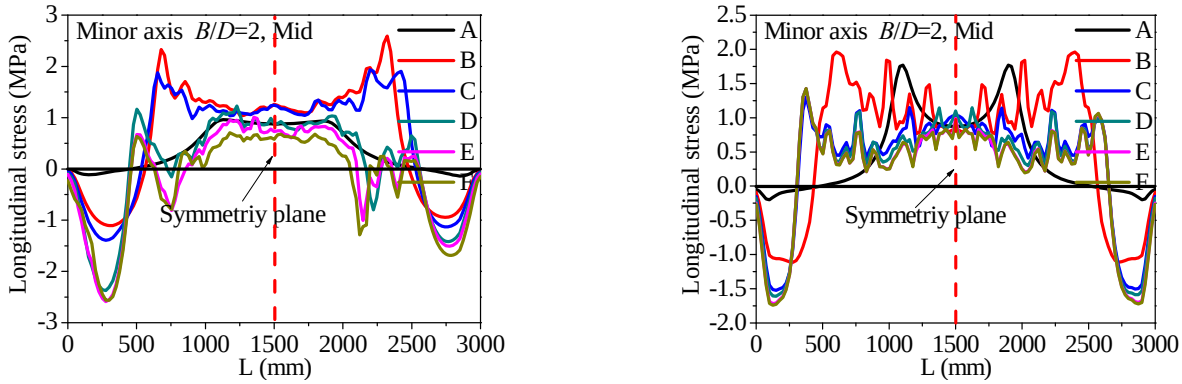

(b) Mid

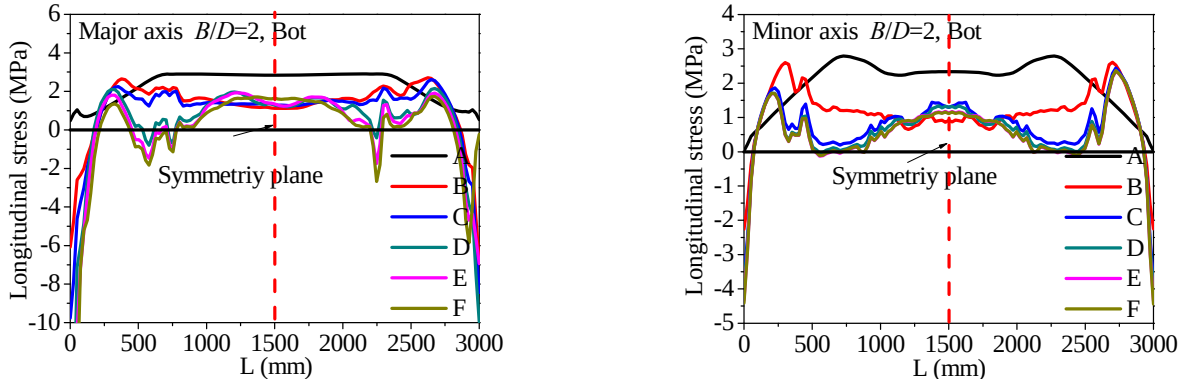

(c) Bot

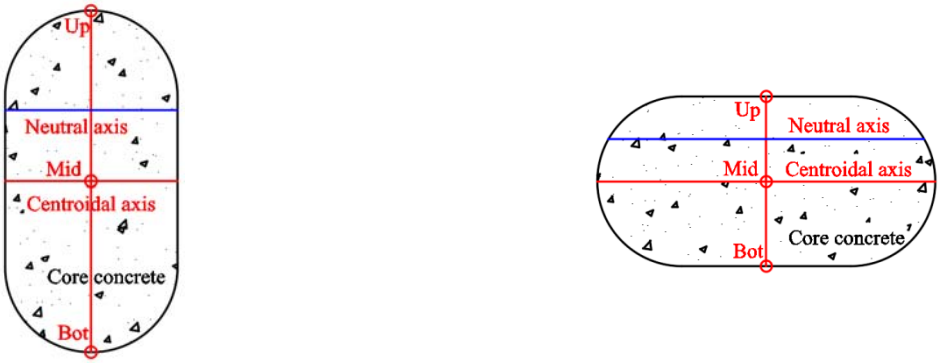

Fig. 21 Development of the longitudinal stress along the length of specimens at different stages

the absolute value of the circumferential strain divided by the axial strain of the steel tube, which reveals the composite effect between the core concrete and steel tube. The core concrete continually expands under loading, mobilizing the steel tube effectively confining the expansion of the concrete due to confinement effect. Besides, stresses of the steel tube are highly affected by the state of the core concrete. The perimeter strain of the steel

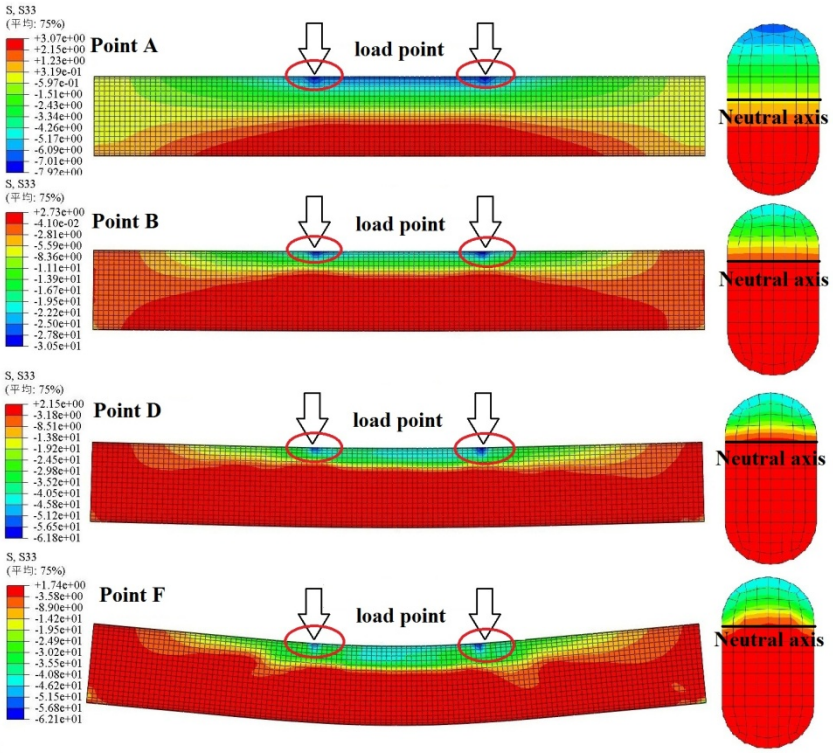

Fig. 22 Development of longitudinal stress distribution in the core concrete

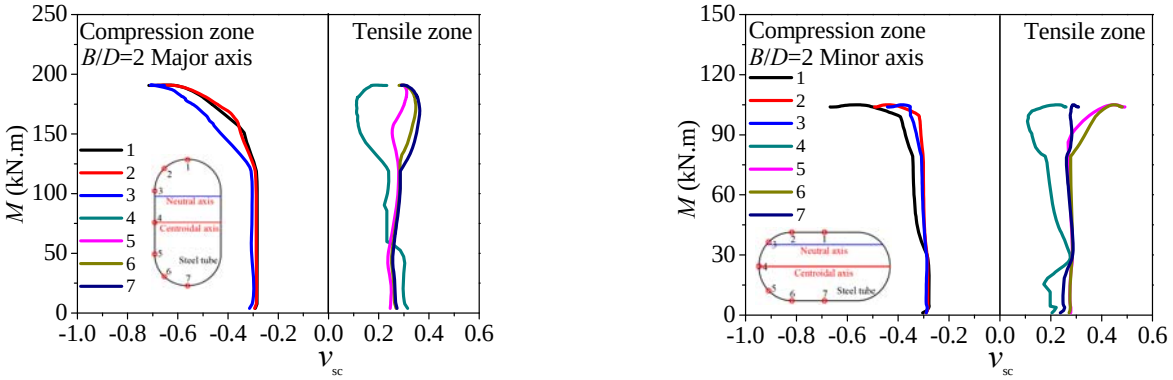

(a) Major axis (b) Minor axis

Fig. 23 Comparison of moment vs. strain ratio curves at different points of the steel tube

tube increases with the expansion of the core concrete, which leads to the increase of the Poisson's ratio of the steel tube. Namely, the more the strain ratio is, the more the confinement effect of the steel tube on the core concrete is. Fig. 23 gives the moment (M) vs. strain ratio (v_{sc}) curves of CFRTs, where the strain ratio is defined as negative in compression zone and positive in tensile zone.

From Fig. 23, it is found that the strain ratio remains constant and approximately equivalent to Poisson's ratio of steel in elastic stage. This implies that the steel tube and core concrete work independently and the confinement effect between the steel tube and core concrete can be neglected. And there is detaching tendency in the interface between the core concrete and steel tube, because the Poisson's ratio of steel is larger than that of concrete. After the steel tube in compression zone reach the yield strength of steel (point C), the strain ratio (points 1 2 and 3) begins to increase remarkably. The change in strain ratio indicates the steel tube starts to produce obvious confinement effect on the core concrete, which results in the core concrete in triple-axial compressive stress, and the peak compressive strength of concrete equals to 62.1 Mpa and 50.3 Mpa, as shown in Fig. 24. However, the strain ratio increases slowly (points 4 and 5) and even decreases (points 3) after reaching the yield of steel in tensile zone (point B), which is regarded that the confinement effect is limited or reduced. The core concrete at point 5 undergoes severs cracking and straining, which is greater than anywhere at the cross-section. At the same time, the cracked concrete in tensile zone still offer strength support to prevent deformation of the steel tube, but contribute little to the flexural capacity of CFRTs due to the concrete severely cracked below the neutral axis. These

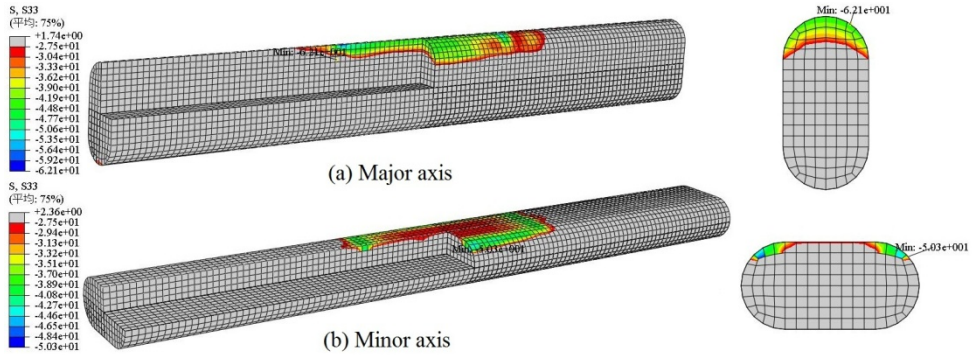

Fig. 24 Maximum longitudinal stress in the core concrete

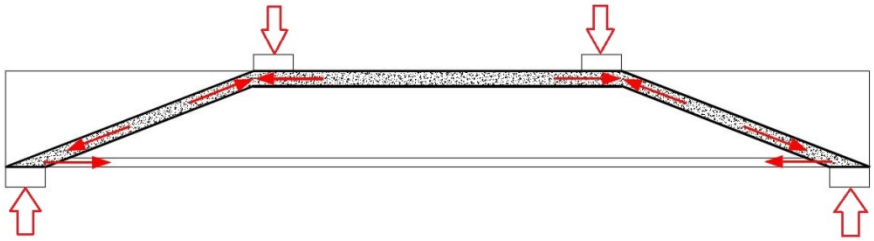

Fig. 25 Tied-arch model on the core concrete

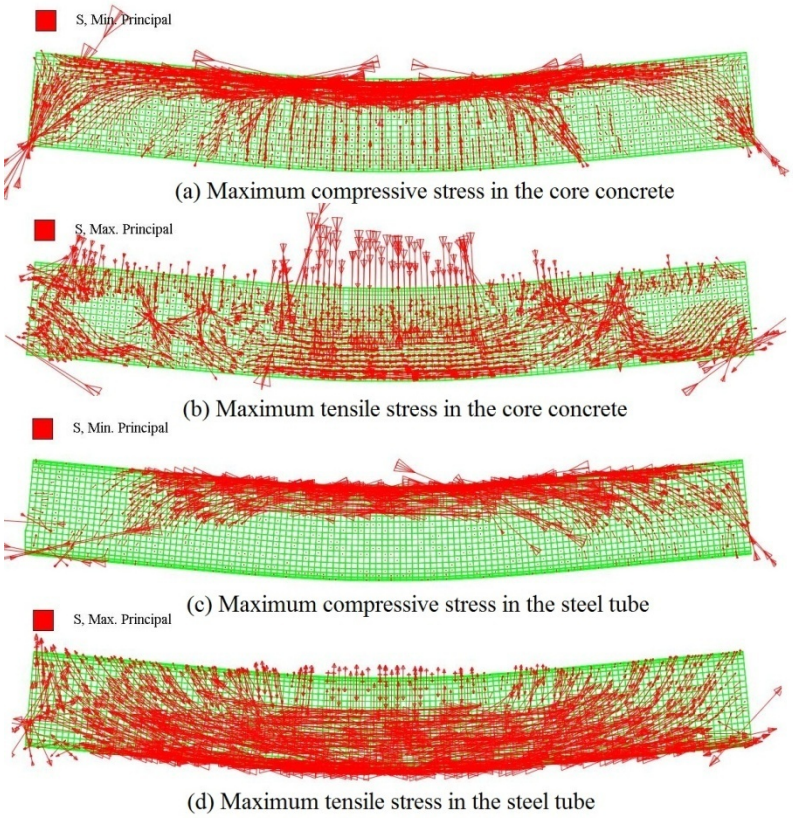

Fig. 26 Maximum stress in CFRT

curves do illustrate trends in the behavior of steel tube during the loading process.

5.5 Load transfer mechanism

A mechanical model of loading transfer in CFT was proposed by Lu and Kennedy (1994), as shown in Fig. 25. In this model, load transfer of the core concrete in the shear span is simplified to a tired arch, which can be verified by the stress distribution extracted from CFRTs in this section.

Fig. 26 gives the typical vector symbol of maximum stress in the core concrete and steel tube, where the arrow,

length and density of the vector symbol represents the direction, magnitude and distribution of the stress, respectively. The load transfer path can be identified by the maximum stress orientation of the core concrete and steel tube in CFRTs. In pure bending and shear span segments, the maximum stress distributes differently. For the core concrete, it can be found from Fig. 26(a) that the maximum compressive stress in concrete is located at the top of the cross-section along the longitudinal direction of CFRT in pure bending segment. Besides, the maximum compressive stress of the core concrete in the shear span is obviously along the line connecting load and support point and distributes in a wider range. The quantity of maximum compressive stress in concrete in pure bending segment is greater than that in the shear span. However, the concrete below the neutral axis is severely cracked and no mechanical means of transfer is provided, as shown in Fig. 26(b). The stress distribution of the core concrete coincide well with the mechanical model (Fig. 25). For the steel tube, it can be seen from Fig. 26(c) that the distribution of the maximum compressive stress in the steel tube in pure bending segment is similar to that in the core concrete, while there is only a little compressive stress in the shear span. Moreover, the maximum tensile stress in the steel tube is situated below the neutral axis in pure bending segment, and there is also strong tensile stress in the shear span which is inclined to longitudinal direction of CFRT, as shown in Fig. 26(d).

The cracks are induced by the tensile stress which is perpendicular to the cracks. For the RC beam, the stirrup is almost no benefit to shear capacity or prevent further propagation of the cracks because the angle between the shear cracks and the stirrup is small. The steel tube in the shear span acts as continuously stirrup to resist the shear force like that in RC beam. The longitudinal continuity in the steel tube makes it much stronger than stirrup in RC beams, which are able to sustain both vertical and longitudinal force in the shear span. The shear force in the shear span is almost sustained by the steel tube rather than the core concrete. The shear stress in the core concrete is under a low level. The orientation of the tensile stress in steel is perpendicular to the crack of the core concrete in the shear span. The steel tube can offer strong restraint to prevent potential shear crack in concrete in the shear span, thus no obvious shear cracking of concrete is observed.

From above analysis, it is concluded that the compressive concrete and both tensile and compressive steel make contribution together to the flexural capacity of CFRTs, whereas cracked concrete contributes slightly due to low tensile stress. In addition, the steel tube in the shear span can effectively sustain shear force and offer strong confinement effect on the core concrete to prevent development of shear crack.

Table 3 Comparison of ultimate moment between experimental, FE and predicted results

Specimen ID	Source	$N_{u,Exp}$	$N_{u,c}$		$N_{u,Exp}/N_{u,c}$	
		Exp	FE	Zhang	FE	Zhang
R-1-3	This paper	54	52	65	1.03	0.82
R-Ma-2-3		176	190	186	0.92	0.95
R-Ma-2-4		217	230	224	0.94	0.97
R-Ma-3-3		355	361	376	0.98	0.95
R-Mi-2-3		100	104	102	0.96	0.98
R-Mi-2-4		126	128	137	0.99	0.93
R-Mi-3-3		185	190	160	1.03	1.16
			Average		0.97	0.96
			COV		0.039	0.103

6. Formula validation

Table 2 gives the formula for the ultimate moment of the CFRTs under bending. The predicted results ($N_{u,c}$) using the corresponding formula are compared to the experimental results ($N_{u,Exp}$), as shown in Table 3, in which the ratios are values of the experimental results divided by the corresponding values. It can be seen that the average ratios of $N_{u,Exp}/N_{u,FE}$ and $N_{u,Exp}/N_{u,Zhang}$ are 0.97 and 0.96 with a coefficient of variation of 0.034 and 0.121, respectively. The FE results are the closest to the experimental results with discrepancies less than 8%. Besides, the predicted results calculated by Ding *et al*. (2017) are in good agreement with the experimental results. Therefore, the method gived by Ding *et al*. (2017) can be adopted as the basic formula to calculate the ultimate moment of the CFRTs.

7. Conclusions

The flexural behavior of CFRTs was investigated through experimental studies and FE analysis. Based on the current experimental and numerical investigations, the following conclusions can be drawn from this paper:

(1) Seven specimens were designed to further investigate the behavior of CFRTs based on the previous research. The CFRTs fail in a very ductile manner. The typical failure modes of CFRTs show

Table 2 Formula for the ultimate moment of the CFRTs under bending

References	Formulation
Ding *et al*. (2017)	$M_u = \gamma^m W_{sc}^M f_{sc,u}$, $\gamma_{maj}^m = \frac{B+0.3D}{2.7B+0.35D} + (1.35-0.054B/D)\Phi$, $\gamma_{min}^m = \frac{B}{6.31B-3.58D} + (1.36+0.16B/D)\Phi$

an outward folding failure mechanism, and the failure shapes are in the shape of a half-sine wave. The local buckling at compression zone results in the crushing of the core concrete. In addition, the parameter analysis clearly demonstrates that both the aspect ratio and steel ratio contribute to enhance the ultimate moment.

(2) FE models are established and verified by experimental results. The reasonable agreement is achieved between FE and experimental results. FE analysis is proposed to investigate the flexural behavior of CFRTs, including the moment vs. curvature curves, the stress and strain distribution in the core concrete and steel tube, the composite action between the core concrete and steel tube and the load transfer mechanism.

(3) Based on the moment vs. curvature curves, the specimens are considered to experience three stages during the loading process: elastic stage, elastic-plastic stage and plastic stage. In addition, there is obvious stress redistribution in the steel tube and core concrete with the increase in load. After reaching the yield of the steel tube in compression zone, the confinement effect of the steel tube on the core concrete increases quickly in compression zone. However, there is barely any confinement in tensile zone after reaching the yield of steel in tensile zone.

(4) Based on the stress distribution extracted from FE model, a comprehensive introduction on the load transfer mechanism in the core concrete and steel tube is carried out.

Acknowledgments

This research work was financially supported by the National Natural Science Foundation of China, Grant No. 51578548 and 51508294, and the National Key Research program of China, Grant No.2017YFC0703404.

References

Aslani, F., Uy, B. and Tao, Z. (2015), "Predicting the axial load capacity of high-strength concrete filled steel tubular columns", *Steel Compos*. *Struct*., *Int*. *J*., **19**(4), 967-993.

~~Aslani, F., Uy, B. and Tao, Z. (2015), "Predicting the axial load capacity of high-strength concrete filled steel tubular columns", *Steel Compos*. *Struct*., *Int*. *J*., **19**(4), 967-993.~~

Chang, X., Ru, Z.L., Zhou, W. and Zhang, Y.B. (2013), "Study on concrete-filled stainless steel carbon steel tubular (CFSCT) stub columns under compression", *Thin-Wall*. *Struct*., **63**(2), 125-133.

Chang, X., Luo, X.L., Zhu, C.X. and Tang, C.N. (2014), "Analysis of circular concrete-filled steel tube support in high ground stress conditions", *Tunn*. *Undergr*. *Sp*. *Tech*., **43**(6), 41-48.

Chang, X., Wang J., Tang, C. and Ru, Z. (2016), "Effects of interface behavior on fracture spacing in layered rock", *Rock Mech*. *Rock Eng*., **49**(5), 1733-1746.

Chen, B.L. and Wang, L.G. (2015), "Experimental study on flexural behavior of splicing concrete-filled gfrp tubular composite members connected with steel bars", *Steel Compos*. *Struct*., *Int*. *J*., **18**(5), 1129-1144.

Chen, J., Wang, J., Xie, F. and Ji, W.L. (2016), "Behavior of thin-walled dodecagonal section double skin concrete-filled steel tubes under bending", *Thin-Wall*. *Struct*., **98**(1), 293-300.

Chitawadagi, M.V. and Narasimhan, M.C. (2009), "Strength deformation behaviour of circular concrete filled steel tubes subjected to pure bending", *J*. *Constr*. *Steel Res*., **65**(5), 1836-1845.

Ding, F.X., Ying, X.Y., Zhou, L.C. and Yu, Z.W. (2011), "Unified calculation method and its application in determining the uniaxial mechanical properties of concrete", *Front*. *Archit*. *Civil Eng*. *China*., **5**(3), 381-393.

Ding, F.X., Fu, L., Yu, Z.W. and Li, G. (2015), "Mechanical performance of concrete-filled steel tubular stub columns with round ends under axial loading", *Thin-Wall*. *Struct*., **97**(12), 22-34.

Ding, F.X., Fu, L., Liu, X.M. and Liu, J. (2016), "Mechanical performances of track-shaped rebar stiffened concrete-filled steel tubular stub columns under axial compression", *Thin-Wall*. *Struct*., **99**(2),168-181.

Ding, F.X., Zhang, T., Wang, L.P. and Fu, L. (2017), "Behavior of concrete-filled round-ended steel tubes under bending", *Steel Compos*. *Struct*., *Int*. *J*., **25**(4), 457-472.

El-Heweity, M.M. (2012), "On the performance of circular concrete-filled high strength steel columns under axial loading", *Alexandria Eng*. *J*., **51**(2), 109-119.

GB 50017-2003, China Standard (2003), Code for design of steel structures, China Planning Press, Beijing, China.

GB/T228-2002, China Standard (2002), Metallic materials-tensile testing at ambient temperatures, Standards Press of China, Beijing, China.

GB/T50081-2002, China Standard (2002), Standard for method of mechanical properties on ordinary concrete, China Building Industry Press, Beijing, China.

Han, L.H., Lu, H., Yao, G.H. and Liao, F.Y. (2006), "Further study on the flexural behavior of concrete-filled steel tubes", *J*. *Constr*. *Steel Res*., **62**(6), 554-565.

Hassanein, M.F. and Kharoob, O.F. (2014), "Analysis of circular concrete-filled double skin tubular slender columns with external stainless steel tube", *Thin-Wall*. *Struct*., **79**(6), 23-37.

Hassanein, M.F., Kharoob, O.F. and Liang, Q.Q. (2013), "Circular concrete-filled double skin tubular short columns with external stainless steel tubes under axial compression", *Thin-Wall*. *Struct*., **73** (12), 252-263.

Hibbitt, Karlson & Sorensen Inc. (2003), ABAQUS/standard User's Manual, Version 6.4.1., Pawtucket, RI, USA.

Karimi, K., Tait, M.J. and El-Dakhakhni, W. (2012), "Influence of slenderness on the behavior of a FRP-encased steel-concrete composite column", *J*. *Compos*. *Constr*.., **16**(1), 100-109.

Kim, J.K., Kwak, H.G. and Kwak, J.H. (2013), "Behavior of Hybrid Double Skin Concrete Filled Circular Steel Tube Columns", *Steel Compos*. *Struct*., *Int*. *J*., **14**(14), 191-204.

Liu, J., Ding, F.X., Liu, X.M. and Yu, Z.W. (2016), "Study on flexural capacity of simply supported steel-concrete composite beam", *Steel Compos*. *Struct*., *Int*. *J*., **21**(4), 829-847.

Lu, Y.Q. and Kennedy, D.J.L. (1994), "The flexural behaviour of concrete-filled hollow structural sections", *Can*. *J*. *Civil Eng*., **21**(1), 111-30.

Moon, J., Roeder, C.W., Lehman, D.E. and Lee, H.E. (2012), "Analytical modeling of bending of circular concrete filled steel tubes", *Eng*. *Struct*., **42**(12), 349-361.

Pagoulatou, M., Sheehan, T., Dai, X.H. and Lam, D. (2014), "Finite element analysis on the capacity of circular concrete-filled double-skin steel tubular (CFDST) stub columns", *Eng*. *Struct*., **72**, 102-112.

Uenaka, K. and Tsunokake, H. (2016), "Concrete filled elliptical steel tubular members with large diameter-to-thickness ratio

subjected to bending", *Structures*, **5**(2) 58-66.
Uenaka, K., Kitoh, H. and Sonoda, K. (2008), "Concrete filled double skin tubular members subjected to bending", *Steel Compos*. *Struct*., *Int*. *J*., **8**(4), 297-312.
Wan, C.Y. and Zha, X.X. (2016), "Nonlinear analysis and design ofconcrete-filled dual steel tubular columns under axial loading", *Steel Compos*. *Struct*., *Int*. *J*., **20**(3), 571-597.
Wang, Q.T. and Chang, X. (2013), "Analysis of concrete-filled steel tubular columns with "T" shaped cross section (CFTTS)", *Steel Compos*. *Struct*., *Int*. *J*., **15**(1), 41-45.
Wang, R.L., Han, H., Nie, J.G. and Zhao, X.L. (2014), "Flexural performance of rectangular CFST members", *Thin-Wall*. *Struct*., **79**(2), 154-165.
Xie, J.X., Cai, C.H., Lu, Z. and Ren, Z.G. (2010), "Test study and numerical simulation of micro-expansive round-ended concrete filled steel tubes coupled column", *Eng*. *J*. *Wuhan Univ*., **43**(4) 485-489. [In Chinese]
Xie, J.X., Lu, Z.A., Tang, P. and Liu, D. (2011), "Modal analysis and experimental study on round-ended CFST coupled column cable stayed bridge, Mechanic Automation and Control Engineering (MACE)", *Proceedings of the 2nd International Conference on IEEE*.
Yuan, W.B. and Yang, J.J. (2013), "Experimental and numerical studies of short concrete-filled double skin composite tube columns under axially compressive loads", *J*. *Constr*. *Steel Res*., **80**(1), 23-31.

CC